Phase shifts and wave-packet displacements in neutron interferometry and a nondispersive, nondefocusing phase shifter

Hartmut Lemmel[1,*] and Apoorva G. Wagh[2]

[1]*Vienna University of Technology, Atominstitut, AT-1020 Wien, Austria and Institut Laue Langevin, FR-38000 Grenoble, France*

[2]*Bhabha Atomic Research Centre, 86 Dhruva, Mumbai 400085, India*

(Received 22 July 2010; published 30 September 2010)

A phase shifter in neutron interferometry creates not only a phase shift but also a spatial displacement of the neutron wave packet, leading to a reduced interference contrast. This wave-packet displacement constitutes a major hindrance in measuring large phase shifts. Here we present a nondispersive configuration with two identical phase shifters placed on one path in successive gaps of a symmetric triple Laue (LLL) interferometer. As compared to a single phase shifter, the dual phase shifter generates double the phase shift, yet a net null displacement of the wave packet. The interferometer thus remains fully focused however large the phase shift or the incident wavelength spread, permitting a white incident neutron beam as in the case of a purely topological phase measurement. Misalignment angles of a monolithic nondispersive dual phase shifter are equal and opposite in the two gaps. Its phase therefore remains nondispersive over a much wider angular range and attains a minimum magnitude at the correct orientation, obviating the need to alternate the phase shifter between the two interferometer paths during its alignment. The setup is hence ideally suited for measuring neutron coherent scattering lengths to ultrahigh precision.

DOI: 10.1103/PhysRevA.82.033626 PACS number(s): 03.75.Dg, 03.65.Vf, 61.05.F−

I. INTRODUCTION

Neutron interferometry affords precise determination of the coherent neutron scattering length b_c of a material from the shift in the interference pattern brought about by a sample of the material inserted in one beam path of the interferometer [1]. We will confine ourselves to the symmetric LLL perfect crystal interferometer which has been the principal workhorse of neutron interferometry. Early experimenters placed the sample with its surface at right angles to the neutron beam (standard configuration). The phase-shift dependence on neutron wavelength as well as the longitudinal displacement of the wave packet reduced the interference contrast for very large phase shifts, hindering precise b_c determination.

Scherm [2] suggested placing the sample with its surface parallel to the Bragg planes of the interferometer. In this configuration, neutrons of each wavelength subtend the corresponding Bragg angle with the sample surface and the phase is exactly wavelength independent (i.e., nondispersive). The sample needs to be aligned to ∼arcsecond precision for this purpose and enables b_c determination to within a few parts in 10^4.

Ioffe and Vrana [3] and Ioffe *et al.* [4] recorded an interferogram each with the nondispersive sample placed on either of the two beam paths of the interferometer. The phase shift between these two interferograms remains nondispersive over a wider (∼arcminute) angular range, reducing the b_c imprecision to a few parts in 10^5.

Wagh and Abbas [5] proposed a comprehensive optimization of this method to attain a further order-of-magnitude improvement in b_c precision and showed that a correction for neutron refraction at the air-sample interfaces would then become mandatory.

We present here a monolithic dual phase shifter in the nondispersive configuration which facilitates a much cleaner measurement, enhancing the b_c precision still further. In addition, the angular alignment of the dual phase shifter turns out to be much simpler compared to the single one.

In Sec. II we compare the phase dispersion in frequently employed sample configurations. In addition to the nondispersive and standard configuration we include the strongly dispersive configuration, which is frequently used for the phase flag and for coherence measurements. Section III recapitulates the phase-shifter formulas and discusses phase shifts and spatial displacements for single and dual phase shifters. In Sec. IV we calculate the phase dispersion originating from dynamical diffraction within the interferometer blades and conclude that the dual phase shifter is much more nondispersive than the single one, thereby extending the magnitude of measurable phases by orders of magnitude. Preliminary b_c measurements with a silicon nondispersive dual phase shifter are described in Sec. V.

II. PHASES AND DISPERSION

Figure 1 depicts the nondispersive (a), standard (b), and strongly dispersive (c) configurations [6] alluded to in the previous section. In all these configurations, the neutron wave packet undergoes not only a phase shift but a spatial displacement as well, as illustrated by the gray bullets in the figure. A large wave-packet displacement causes a drop in the interference contrast [7], allowing characterization of longitudunal and transverse coherence lengths of the neutron beam [8].

The right column in Fig. 1 displays the dependence of the phase shift $\chi = \chi_{II} - \chi_I$ on the misalignment angle ε. In the standard configuration (b), the exact alignment setting ($\varepsilon = 0$) can be determined easily from the phase measurement itself as the phase is symmetric about $\varepsilon = 0$. This possibility does not exist for the nondispersive configuration (a), though the alignment is required to be more precise (∼arcsecond).

*hartmut@lemmel.at

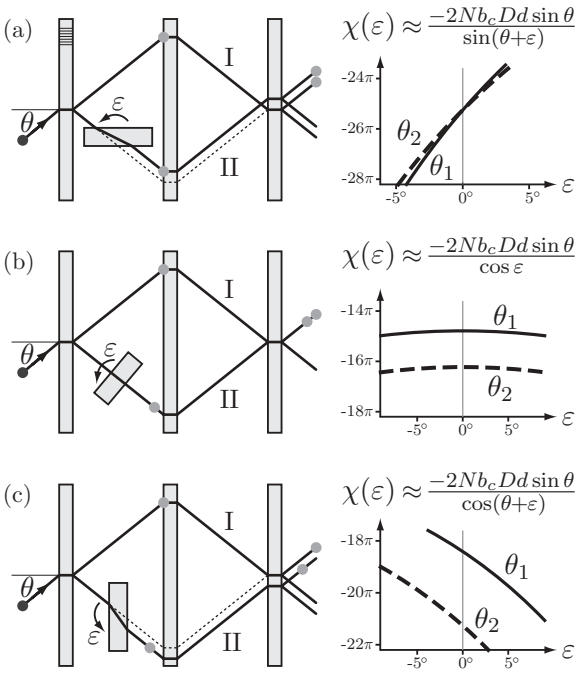

FIG. 1. Sample configurations in nondispersive (a), standard (b), and strongly dispersive (c) geometry. The bullets along the beam paths compare the positions of wave packets in paths I and II at certain times. The phase shift χ is plotted versus misalignment angle ε calculated for a 1-mm silicon phase shifter and two different Bragg angles $\theta_1 = 36^\circ$ and $\theta_2 = 40^\circ$.

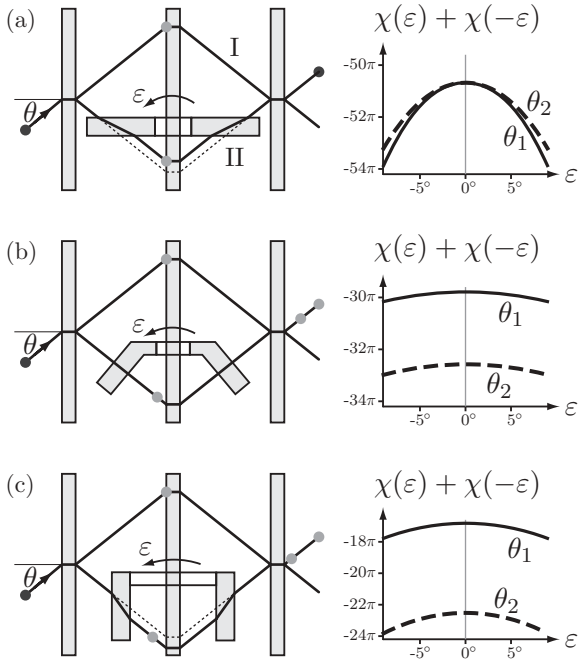

FIG. 2. Setups for measuring the sum $\chi(\varepsilon)+\chi(-\varepsilon)$ for the phase-shifter geometries explained in Fig. 1.

On alternating the nondispersive sample between the two beam paths of the interferometer at each ε [3,4], the phase shift $\chi(\varepsilon) - [-\chi(-\varepsilon)]$ between the interferograms for the two paths is symmetric about $\varepsilon = 0$, attaining a minimum magnitude at the correct alignment which only needs ~arcminute accuracy [cf. Fig. 2(a)].

To augment the precision of this method still further, we propose here a dual nondispersive phase shifter comprising two identical and parallel phase shifters placed on one path, one before and the other after the mirror blade [Fig. 2(a)], in the nondispersive configuration. The phase shift $\chi(\varepsilon) + \chi(-\varepsilon)$ can now be obtained in a single measurement with this dual phase shifter placed on a single beam path. (The situation $\chi(\varepsilon) - \chi(-\varepsilon)$ is shown in Fig. 3 for completeness.) The parallelity and identical thicknesses of the samples can be most easily attained by monolithic construction. The effective thickness of the phase shifter is doubled, resulting in higher interference order and even better accuracy. Furthermore, the spatial displacement of the wave packet effected by the sample in the first gap is exactly annulled in the second. The wave packets arriving from the two beam paths always fully overlap, that is, they reach the analyzer blade at the same time and same position, regardless of the magnitude of the phase shift or the incident neutron wavelength. This large nondispersive phase and the concomitant null spatial shift of the wave packet yields full interference contrast even with a white, and hence high-intensity, incident neutron beam, enabling a fast and precise measurement. The situation is akin to that for the observation [9] of the purely topological (and hence nondispersive) Aharonov-Bohm phase [10].

III. CALCULATIONS

A. Phase shift

If a plane wave $\psi_{\text{in}} = e^{i\vec{k}\cdot\vec{r}}$ traverses a material slab of thickness D, the transmitted wave is given by $\psi_{\text{out}} = e^{i\chi}\psi_{\text{in}}$ with the phase shift $\chi = D(K_\perp - k_\perp)$, with $K_\perp$ and $k_\perp$ denoting the wave vector components (inside and outside, respectively) perpendicular to the surface (see Fig. 4). The total energy of the neutron must be conserved:

$$E = \frac{k^2\hbar^2}{2m} + V_{\text{air}} = \frac{K^2\hbar^2}{2m} + V, \tag{1}$$

where V denotes the neutron optical potential of the phase shifter $V = 2\pi\hbar^2 N b_c/m$, with the neutron mass m, atomic density N, and coherent neutron scattering length b_c. V_{air} is the neutron optical potential for air, which can usually be neglected but is included here for completeness. This yields the (relative) index of refraction

$$n = \frac{K}{k} = \sqrt{1 - \frac{V - V_{\text{air}}}{E - V_{\text{air}}}}. \tag{2}$$

For thermal neutrons and virtually all materials the condition $E \gg |V| \gg |V_{\text{air}}|$ applies and n is very close to unity: $n \approx 1 - \lambda^2 N b_c/2\pi$.

With $K_\parallel = k_\parallel = k\sin\varphi$ and $K_\perp = \sqrt{K^2 - K_\parallel^2} = \sqrt{n^2k^2 - k_\parallel^2}$ we obtain the phase shift

$$\chi = D(K_\perp - k_\perp) = Dk(\sqrt{n^2 - \sin^2\varphi} - \cos\varphi). \tag{3}$$

A first-order series expansion by n around 1 gives

$$\chi \approx -Dk\frac{1-n}{\cos\varphi} \approx -Dk\frac{V/E}{2\cos\varphi} = -\frac{Nb_cD\lambda}{\cos\varphi}. \tag{4}$$

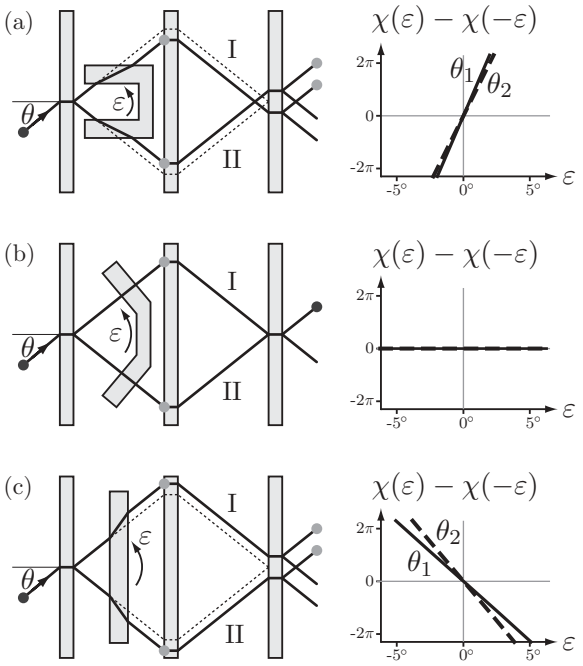

FIG. 3. Setups for measuring the difference $\chi(\varepsilon) - \chi(-\varepsilon)$ for the phase-shifter geometries explained in Fig. 1.

For the nondispersive geometry [Fig. 1(a)], $\varphi = \pi/2 - \theta$. Here θ stands for the interferometer Bragg angle for neutrons of wavelength $\lambda = 2d \sin\theta$, with d denoting the Bragg planar spacing of the interferometer crystal. Inserting (1) and (2) in Eq. (3), we obtain

$$\chi = \frac{D\pi}{d}\left(\sqrt{1 - \frac{2md^2(V - V_{\text{air}})}{\hbar^2\pi^2}} - 1\right), \tag{5}$$

which is exactly nondispersive. A misalignment of the phase shifter by a few arcseconds however makes the phase slightly dispersive [cf. plots in Fig. 1(a)]. Over the finite angular width of the interferometer Laue reflection, deviations from exact Bragg incidence introduce a minute dispersion in the phase, which is discussed in Sec. IV.

If the phase shifter is misaligned by an angle ε, $\varphi = \pi/2 - (\theta + \varepsilon)$. Then $\cos\varphi = \sin(\theta + \varepsilon)$ in Eq. (4) and the approximate phase becomes

$$\chi(\varepsilon) \approx -\frac{Nb_c D\lambda}{\sin(\theta+\varepsilon)} = -\frac{2Nb_c Dd\sin\theta}{\sin(\theta+\varepsilon)}. \tag{6}$$

In addition to the rotation ε about the vertical axis we consider a tilt γ of the phase shifter about a horizontal axis parallel to its surface. The tilt changes the phase shift by a factor of $1/\cos\gamma$ [8].

For the nondispersive dual phase shifter configuration [Fig. 2(a)], the misalignment angles are equal and opposite in the two gaps of the interferometer, yielding a total phase

$$\chi_d(\varepsilon) = \chi(\varepsilon) + \chi(-\varepsilon) \tag{7}$$

$$= -\frac{2Nb_c Dd}{\cos\gamma}\left(\frac{\sin\theta}{\sin(\theta+\varepsilon)} + \frac{\sin\theta}{\sin(\theta-\varepsilon)}\right) \tag{8}$$

$$\approx 2\chi(0)[1 + \varepsilon^2(\cot^2\theta + 1/2)](1 + \gamma^2/2). \tag{9}$$

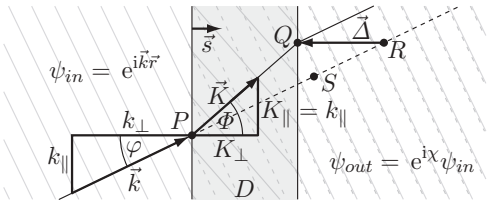

FIG. 4. A plane wave passing a phase shifter.

Since the first-order terms in the misalignment angles cancel out here, the phase for the dual phase shifter remains nondispersive over a wider (∼arcminute) range of incidence angles [cf. plots in Fig. 2(a)]. In contrast to the single nondispersive phase shifter, which needs to be alternated between the two paths in the interferometer at each angular setting [4] for alignment, the dual phase shifter can be aligned while placed on one path of the interferometer due to the quadratic variation of its phase with both the misalignment angles.

B. Spatial shift of the wave packet

We have just derived the phase shift of a single plane wave. We now consider a Gaussian wave packet with the central wave component $\vec{k}$. The center of the wave packet's envelope travels the classical path $\overline{PQ}$ shown in Fig. 4. An undisturbed wave packet (with no phase shifter) would propagate along the dashed path $\overline{PR}$ and reach the point R at the same time the disturbed wave packet reaches Q. This follows from the fact that both wave packets always have the same $r_\parallel$ position because $k_\parallel = K_\parallel$. The wave packet thus undergoes the displacement $\vec{\Delta}$ from R to Q, which is always perpendicular to the phase shifter surface. With the unit surface normal vector $\vec{s}$, $D\vec{s}/K_\perp = (D\vec{s} - \vec{\Delta})/k_\perp$ and

$$\vec{\Delta} = -\vec{s}D\left(\frac{k_\perp}{K_\perp} - 1\right) = -\vec{s}D\left(\frac{\cos\varphi}{\sqrt{n^2 - \sin^2\varphi}} - 1\right). \tag{10}$$

The spatial shift can be accompanied by both a time lag of the wave packet and a transverse displacement of the beam, the latter defocusing the interferometer as the two beam paths do not meet at the entrance face of the analyzer blade. The terms "transverse" and "longitudinal" are used ambiguously in the literature, sometimes relative to the beam direction and at other times relative to the Bragg planes. In this paper, we resolve $\vec{\Delta}$ into two nonorthogonal components, the defocusing component f perpendicular to the Bragg planes and the delaying component l parallel to the beam. Figure 5 depicts this decomposition in the three cases of nondispersive, standard, and strongly dispersive configurations. The former two are purely defocusing and delaying, respectively, while the latter is a mixture of both. Using this prescription, we can easily add up the respective components of $\vec{\Delta}$ due to several phase shifters placed in various sections of the interferometer and arrive at the net effect. The results are displayed in Figs. 1–3. The interferometer is focused if neutrons from both beam paths reach the third interferometer blade at the same position. The time lag is zero if the wave packets reach the third blade simultaneously. Gray bullets in the figures indicate simultaneous wave-packet positions on the two paths. All configurations of $\chi(\varepsilon)+\chi(-\varepsilon)$ [Figs. 2(a) to 2(c)] and all

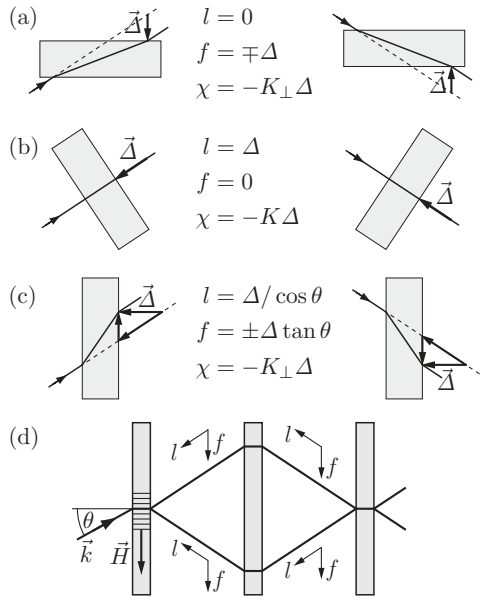

FIG. 5. Decomposition of the spatial shift $\vec{\Delta}$ into defocusing f and lag distance l for different phase-shifter geometries (a) to (c). The orientations of the f and l axes for different sample positions are shown in (d).

phase shifters perpendicular to the beam [Figs. 1 to 3(b)] are fully focused ($f = 0$). On the other hand, all configurations of $\chi(\varepsilon)-\chi(-\varepsilon)$ [Figs. 3(a) to 3(c)] and all nondispersive configurations [Figs. 1 to 3(a)] have no time lag ($l = 0$). A complete overlap of the wave packets ($f = 0$ and $l = 0$) occurs in configurations Figs. 3(b) and 2(a). While the former is the trivial case with zero phase shift ($\chi = 0$) the latter generates double the phase shift with a null wave-packet displacement as already described.

The spatial shift $\vec{\Delta}$ and phase shift χ (3) are related as

$$\vec{K}\cdot\vec{\Delta} = -K_\perp D\left(\frac{k_\perp}{K_\perp} - 1\right) = D(K_\perp - k_\perp) = \chi. \quad (11)$$

In the nondispersive dual phase shifter configuration [Fig. 2(a)] the equal and opposite spatial shifts $\vec{\Delta}$ in the two gaps of the interferometer cancel out and yield a null defocusing. However, since $K_\perp$ also reverses sign in the second gap, $\chi = \vec{K}\cdot\vec{\Delta}$ has the same sign in both gaps and adds up.

Some authors identify the product $\vec{k}\cdot\vec{\Delta}$ with the phase shift χ [1,8]. However, this holds as an approximation only for n very close to unity. In general,

$$\vec{k}\cdot\vec{\Delta} = Dk\cos\varphi\left(1 - \frac{\cos\varphi}{\sqrt{n^2-\sin^2\varphi}}\right) = \chi\frac{\cos\varphi}{\sqrt{n^2-\sin^2\varphi}} \quad (12)$$

differs from χ. Even for normal incidence ($\varphi = 0$) where $K_\perp$ and $k_\perp$ are the closest to each other,

$$\vec{k}\cdot\vec{\Delta} = kD(1-1/n) = \chi/n, \quad (13)$$

$$\vec{K}\cdot\vec{\Delta} = nk\Delta = kD(n-1) = \chi. \quad (14)$$

A tilt γ of the phase shifter about the horizontal axis creates a vertical defocusing $\vec{h}$. We can take Fig. 4 as a vertical cut

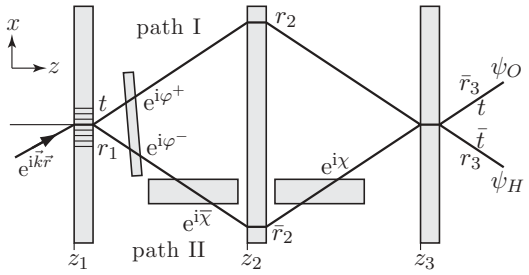

FIG. 6. Interferometer setup. For calculating the exiting wave functions ψ_O and ψ_H all factors indicated along the beam paths have to be collected.

through the phase shifter and replace φ by γ. Then $\vec{h}$ equals $\overrightarrow{SQ}$, that is,

$$\vec{h} = \vec{\Delta}\sin\gamma \approx -\vec{z}D\frac{1-n}{\cos^2\gamma}\sin\gamma \approx -\vec{z}\frac{Nb_cD\lambda^2\tan\gamma}{2\pi\cos\gamma}. \quad (15)$$

With the nondispersive dual phase shifter [Fig. 2(a)] the net vertical shift also becomes zero.[1]

IV. LIMITS OF NONDISPERSION

How nondispersive is the "nondispersive" configuration? The phase shift depends on k_x, which is the wave vector component perpendicular to the phase shifter surface (cf. Fig. 6):

$$\chi = D(K_x - k_x), \quad (16)$$

$$K_x = \sqrt{k_x^2 - 2m(V - V_{\rm air})/\hbar^2}. \quad (17)$$

The k_x distribution, determined by the interferometer crystal, is centered at $k_{xB} = H/2 = \pi/d$, with d denoting the Bragg planar spacing and H the magnitude of the corresponding reciprocal lattice vector. Using the deviation from the exact Bragg law $\delta k_x = k_x - k_{xB}$, we express the phase shift (16) as a series expansion in powers of $\delta k_x/k_{xB}$ as

$$\chi = \chi_B\left[1 - \frac{\delta k_x}{n_x k_{xB}} + \frac{1+\frac{1}{n_x}}{2}\frac{\delta k_x^2}{n_x^2 k_{xB}^2} - O\frac{\delta k_x^3}{k_{xB}^3}\right], \quad (18)$$

with $\chi_B = D(K_{xB} - k_{xB})$ and $n_x = K_{xB}/k_{xB}$.

The k_x distribution is delineated by the theory of dynamical diffraction [1,6,11,12], which we will use in the next paragraphs to determine the phase dispersion $\delta\chi/\chi_B$ as well as the resulting contrast of the interference fringes. The phase dispersion turns out to be in the order of 10^{-5} for a single phase shifter. With the dual phase shifter all odd power terms in this series cancel out, leaving a dispersion of $\sim 10^{-10}$.

A. Single beam splitter

The interferometer consists of identical crystal slabs in symmetric Laue geometry. Each crystal slab splits an incoming plane wave into two components, a transmitted and a reflected one [see Fig. 7(a)]. The reflection coefficient depends on the

[1]The $\cos\gamma$ term in the denominator of Eq. (15) is missing in [8] Eq. (27) and [1] Eq. (4.43).

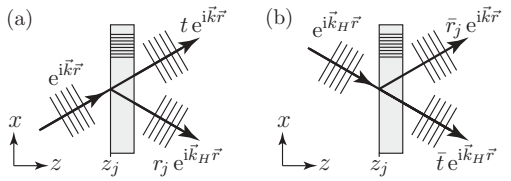

FIG. 7. Geometry of symmetric Laue reflection.

blade position z_j (Fig. 7) and is therefore denoted by r_j. We adapt the notation of [13] and express r_j and the transmission coefficient t as

$$t = \exp[i(-A_0 - A_H y)]\left\{\cos(A_H\sqrt{1+y^2}) + \frac{iy}{\sqrt{1+y^2}}\sin(A_H\sqrt{1+y^2})\right\}, \tag{19}$$

$$r_j = \exp[i(-A_0 + A_H y + 2A_H y z_j/D_0)]\sqrt{\frac{V_H}{V_{-H}}} \times \frac{-i}{\sqrt{1+y^2}}\sin(A_H\sqrt{1+y^2}), \tag{20}$$

$$A_{0,H} = \frac{D_0 k}{2\cos\theta_B}\frac{|V_{0,H}|}{E}. \tag{21}$$

D_0 denotes the blade thickness, $V_{0,H}$ the crystal potentials, and E the neutron energy. The parameter y is a dimensionless scaled deviation from the exact Bragg incidence and can be expressed in terms of either the misset angle $\delta\theta$ or in terms of δk_x as

$$y = -\frac{\hbar^2 k_{xB}}{m|V_H|}\delta k_x = -\frac{1}{X}\frac{\delta k_x}{k_{xB}}, \quad \delta k_x = k_x - k_{xB}, \tag{22}$$

$$y \approx -\frac{\sin 2\theta_B}{|V_H|/E}\delta\theta, \quad \delta\theta = \theta - \theta_B. \tag{23}$$

X is half the ratio between the reflecting crystal potential V_H and the kinetic energy $\hbar^2 k_{xB}^2/(2m)$ of the x component. Both depend solely on parameters of the interferometer crystal since $k_{xB} = \pi/d$:

$$X = \frac{m|V_H|}{\hbar^2 k_{xB}^2} = \begin{cases} 0.485\times10^{-5} & \text{for Si 220,} \\ 1.297\times10^{-5} & \text{for Si 111.} \end{cases} \tag{24}$$

The wave vector $\vec{k}$ of the transmitted component behind the crystal is identical to the incident one since the incidence and exit surfaces of the crystal slab are parallel. The wave vector $\vec{k}_H$ of the reflected component is calculated quite easily for the symmetric Laue case. The component k_x being parallel to the crystal surface is left unchanged when entering or exiting the crystal. Inside the crystal, k_x's of the reflected and incident waves differ by the reciprocal lattice vector magnitude $H = 2\pi/d = 2k_{xB}$. Thus $k_{Hx} = k_x - H$ and the z component follows from energy conservation, that is, $k_{Hz} = \sqrt{k^2 - k_{Hx}^2}$:

$$\vec{k} = \begin{pmatrix} k_x \\ k_z \end{pmatrix} = \begin{pmatrix} k_{xB} + \delta k_x \\ k_z \end{pmatrix} = k\begin{pmatrix} \sin(\theta_B + \delta\theta) \\ \cos(\theta_B + \delta\theta) \end{pmatrix}, \tag{25}$$

$$\vec{k}_H = \begin{pmatrix} k_{Hx} \\ k_{Hz} \end{pmatrix} = \begin{pmatrix} k_x - H \\ k_{Hz} \end{pmatrix} = \begin{pmatrix} -(k_{xB} - \delta k_x) \\ \sqrt{k^2 - k_{Hx}^2} \end{pmatrix} \tag{26}$$

$$\approx k\begin{pmatrix} -\sin(\theta_B - \delta\theta) \\ \cos(\theta_B - \delta\theta) \end{pmatrix} \tag{27}$$

This brings out an important feature of Laue reflection: Incidence and exit angles are not equal. For an incidence angle $\theta_B + \delta\theta$, the forward diffracted and diffracted beams exit at angles $\theta = \theta_B + \delta\theta$ and $\theta_B - \delta\theta$, respectively. The equal and opposite deviations from θ_B of the two exiting beams also follow directly from the continuity of the tangential component of the respective wave vector across the crystal-air interface [12]. Consequently, the parameters y, $\delta\theta$, and δk_x change sign after every reflection. We will denote this sign change by barred symbols: $\bar{r}_j = r_j(-y)$, $\bar{t} = t(-y)$, $\bar{\chi} = \chi(-\delta k_x)$. These symbols have to be used whenever the beam travels in the $\vec{k}_H$ direction [see Fig. 7(b)].

B. Whole interferometer

Figure 6 shows the whole interferometer with the sample and auxiliary phase flag. We take a single plane-wave component $\exp(i\vec{k}\cdot\vec{r})$ of the incident beam and calculate the exiting O wave component $\psi_O = \psi_{OI} + \psi_{OII}$, which consists of contributions from both beam paths. Along each beam path each crystal blade contributes by a reflection or transmission factor as described earlier. The sample and phase flag contribute by phase factors. (We neglect absorption.) After the first reflection we have to use the barred symbols, after the second reflection the unbarred terms, etc.:

$$\psi_{OI} = \exp(i\vec{k}\vec{r})t\exp(i\varphi^+)r_2\bar{r}_3, \tag{28}$$

$$\psi_{OII} = \exp(i\vec{k}\vec{r})r_1\exp(i\varphi^-)\exp(i\bar{\chi})\bar{r}_2\exp(i\chi)t. \tag{29}$$

The intensity of the O beam then becomes

$$I_O = |\psi_{OI} + \psi_{OII}|^2 = a[1 + \cos(\chi_d - \delta\varphi)]. \tag{30}$$

In the last step we have used the fact that $r_2\bar{r}_3 = r_1\bar{r}_2$. $\delta\varphi = \varphi^+ - \varphi^-$ is the known contribution of the auxiliary phase flag and $\chi_d = \chi + \bar{\chi}$ is the total phase shift of the dual phase shifter to be measured in the experiment. The symbol a stands for the O intensity (averaged over the interference fringes) for a given misset parameter y, that is,

$$a = 2|tr_2\bar{r}_3|^2 \tag{31}$$

$$= \frac{2\sin^4(A_H\sqrt{1+y^2})}{(1+y^2)^2} - \frac{2\sin^6(A_H\sqrt{1+y^2})}{(1+y^2)^3}, \tag{32}$$

and is plotted in Fig. 8. The parameter A_H determines the number of intensity oscillations in a given y interval but leaves the envelope unaffected. It can be shown that the envelope is

$$\begin{cases} \frac{8}{27} & \text{for } |y| \leqslant 1/\sqrt{2}, \\ \frac{2}{(1+y^2)^2} - \frac{2}{(1+y^2)^3} & \text{for } |y| > 1/\sqrt{2}, \end{cases} \tag{33}$$

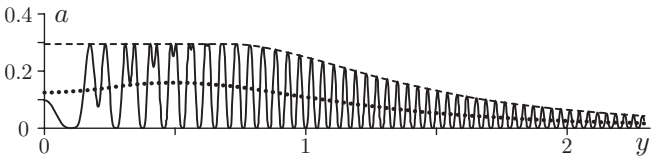

FIG. 8. Typical plot of the average O beam intensity versus y for $A_H = 100$. The distribution is symmetric about $y = 0$. The dotted line shows the distribution after averaging the A_H oscillations.

with the half-width $\delta y = \sqrt{2}$. With (22) the corresponding wavelength dispersion reads $\delta k_x/k_{xB} = -X\delta y$ and is in the order of 10^{-5}. We also express the phase shift χ, Eq. (18), in terms of y:

$$\chi = \chi_B + vy + wy^2 + O(Xy)^3, \tag{34}$$

$$v = \chi_B \frac{X}{n_x} \approx \chi_B \cdot 10^{-5}, \tag{35}$$

$$w = \chi_B \frac{X^2}{2}\left(\frac{1}{n_x^2} + \frac{1}{n_x^3}\right) \approx \chi_B \cdot 10^{-10}. \tag{36}$$

For the single phase shifter we obtain a phase dispersion of $\delta\chi/\chi_B \approx \delta y X/n_x \approx 10^{-5}$, as n_x is close to unity. For the dual phase shifter the total phase shift reads

$$\chi_d = \chi + \bar{\chi} = \chi(y) + \chi(-y) \approx 2\,\chi_B + 2\,wy^2. \tag{37}$$

The sign change of y due to the Laue reflection cancels all odd terms of the series expansion (34), resulting in a phase dispersion of $\delta\chi/\chi_B \approx (\delta y X/n_x)^2 \approx 10^{-10}$.

C. Contrast

The phase dispersion within the wave packet creates a drop of interference contrast, which we calculate for the single and dual phase shifter case, the former already given by Petrascheck [6]. The contrast is determined by the remaining amplitude of interference fringes after integrating (30) over all components of the y distribution. To solve the integral we first replace the sine oscillations in (32) by their average, i.e., $\langle\sin^4(\cdot)\rangle \to 3/8$, $\langle\sin^6(\cdot)\rangle \to 5/16$. This is justified as A_H depends on wavelength and Bragg angle and strongly varies within the beam divergence. Then

$$\langle a\rangle = \frac{2\langle\sin^4(\cdot)\rangle}{(1+y^2)^2} - \frac{2\langle\sin^6(\cdot)\rangle}{(1+y^2)^3} = \frac{1+6y^2}{8(1+y^2)^3}. \tag{38}$$

The phase shift of each y component is given by (34). For the single phase shifter case we drop the second order and set $\chi_s = \chi_B + vy$. The integrated intensity reads

$$I_s = \int_{-\infty}^{\infty} \frac{1+6y^2}{8(1+y^2)^3}[1+\cos(\chi_B + vy - \delta\varphi)]dy \tag{39}$$

$$= \frac{9\pi}{64}[1 + c_s\cos(\chi_B - \delta\varphi)] \tag{40}$$

with the contrast

$$c_s = \left|e^{-|v|}\left(1 + |v| - \tfrac{5}{9}v^2\right)\right| \approx \exp\left(-\tfrac{19}{18}v^2\right). \tag{41}$$

The approximation is valid for thermal neutrons where

$$v = \frac{\chi_B X}{n_x} = \frac{\pi\Delta}{\Delta_0 \tan\theta_B} \ll 1, \tag{42}$$

meaning that $\chi_B \ll n_x/X \approx 10^5$ or that the spatial displacement $\Delta \ll \Delta_0$. The so-called Pendellösung length Δ_0 is in the order of 30 to 50 μm.

In the dual phase shifter case the phase shift is given by (37). The integral can be solved with MATHEMATICA after expressing the cosine as the real part of the exponential function:

$$I_d = \int_{-\infty}^{\infty} \frac{1+6y^2}{8(1+y^2)^3}[1+\cos(2\chi_B + 2wy^2 - \delta\varphi)]\,dy \tag{43}$$

$$= \mathrm{Re}\int_{-\infty}^{\infty} \frac{1+6y^2}{8(1+y^2)^3}[1 + e^{i(2\chi_B + 2wy^2 - \delta\varphi)}]dy \tag{44}$$

$$= \mathrm{Re}\left\{\frac{9\pi}{64}\left[1 + f\left(\sqrt{\frac{2w}{i}}\right)e^{i(2\chi_B - \delta\varphi)}\right]\right\} \tag{45}$$

$$= \frac{9\pi}{64}[1 + c_d\cos(2\chi_B + \xi_d - \delta\varphi)]. \tag{46}$$

The function

$$f(x) = \frac{2}{\sqrt{\pi}}\left(x + \frac{10}{9}x^3\right) - \left(\frac{28}{9}x^2 + \frac{20}{9}x^4 - 1\right)e^{x^2}\,\mathrm{erfc}\,x \tag{47}$$

taken with the complex argument $x = \sqrt{2w/i} = \sqrt{2w}e^{-i\pi/4}$ gives both contrast c_d and phase defect ξ_d:

$$c_d = \left|f\left(\sqrt{\frac{2w}{i}}\right)\right| \approx \exp\left(-\frac{128}{9\sqrt{\pi}}|w|^{3/2}\right), \tag{48}$$

$$\xi_d = \arg f\left(\sqrt{\frac{2w}{i}}\right) \approx \frac{38}{9}w. \tag{49}$$

The approximations are again valid for thermal neutrons where $w \ll 1$.

The results are plotted in Fig. 9. To bring about the same loss in contrast as a single phase shifter, a dual phase shifter has to introduce at least five orders of magnitude larger phase.

As opposed to the single phase shifter case, the contrast drop of the dual phase shifter is governed primarily by large y components. Their intensity is small (cf. Fig. 8) but their impact on the contrast is large as their phase contribution is proportional to y^2. In real-life experiments, however, large y components may not at all be presented to the interferometer crystal, depending on the monochromator in use. We take that into account by multiplying the integrand in (43) with a Gaussian envelope $\exp[-y^2/(2\sigma^2)]/\sqrt{2\pi\sigma^2}$. The contrast and phase defect then read

$$c_d = \left|\frac{f\left(\sqrt{\frac{2w}{i} + \frac{1}{2\sigma^2}}\right)}{f\left(\sqrt{\frac{1}{2\sigma^2}}\right)}\right| \tag{50}$$

$$\approx \exp\left\{-\frac{16}{3}w^2\left[\sqrt{\left(\frac{143}{27}\right)^2 + \frac{8\sigma^2}{\pi}} - \frac{143}{27}\right]\right\}, \tag{51}$$

$$\xi_d = \arg\frac{f\left(\sqrt{\frac{2w}{i} + \frac{1}{2\sigma^2}}\right)}{f\left(\sqrt{\frac{1}{2\sigma^2}}\right)} \approx \frac{38}{9}w\exp\left(-\frac{2}{\sigma}\right). \tag{52}$$

The contrast is plotted for different values of σ in the lower part of Fig. 9. For a finite σ, the contrast loss exhibits a w^2 proportionality for small phase shifts in accordance with the

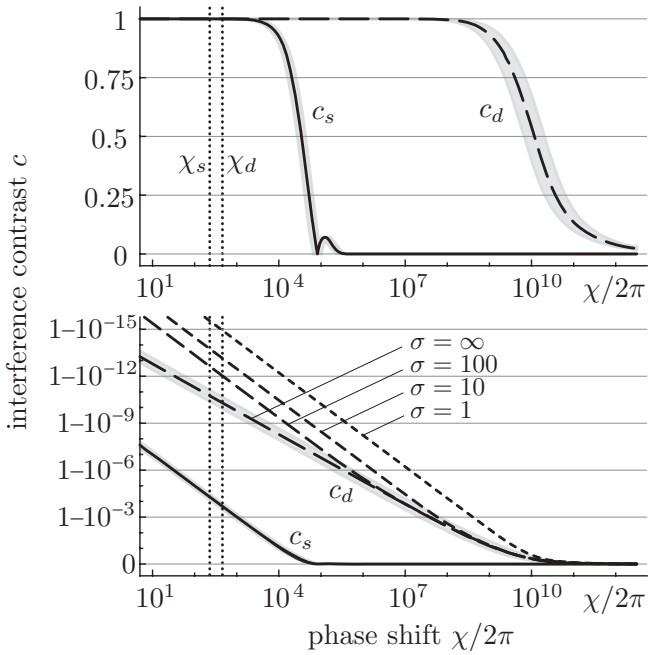

FIG. 9. Contrast of single (c_s) and dual (c_d) phase shifters versus phase shift in linear (top) and logarithmic view (bottom). The gray-shaded regions show variations with the index of refraction n_x ranging between 0.8 and 1.25. The dotted lines indicate single and dual phase shifts for our experimental parameters (18-mm-thick silicon and 220 silicon interferometer). The dependence of c_d on the width of the k_x distribution incident on the interferometer is illustrated by four different Gaussian widths σ (in units of the y parameter).

approximation (51), but beyond a sufficiently large phase shift, it switches to the curve (48) with $w^{3/2}$ dependence. The regime of thermal neutron experiments is in the region of the dotted lines in Fig. 9. The lines indicate the single and dual phase shifts of an 18-mm-thick silicon sample with a 220 silicon interferometer, used in our experiment (cf. next section). The contrast drop amounts to 5×10^{-5} for the single phase shifter and—depending on the monochromator—10^{-11} to 10^{-15} for the dual one. Much larger variations may however be observed with larger interferometers (giving room for thicker phase shifters) or interferometers for cold neutrons [14] when they become available.

The second-order calculation for the dual phase shifter yields a phase defect ξ_d by which the measured phase differs from the desired phase $2\chi_B$ [cf. (46)]. The second-order terms in the χ distribution (34) are equal for positive and negative y components and add together. The single phase shifter shows a similar phase defect if the second-order term is taken into account. As we have verified by numerical calculations, the relative phase defect ξ/χ is equal for single and dual phase shifter in the regime of thermal neutrons and can be approximated as

$$\frac{\xi_s}{\chi_s} \approx \frac{\xi_d}{\chi_d} \approx \frac{19}{9}X^2 = \begin{cases} 0.50 \times 10^{-10} & \text{for Si 220,} \\ 3.6 \times 10^{-10} & \text{for Si 111.} \end{cases} \tag{53}$$

It is many orders of magnitude below current limits of measurement accuracy and can be neglected.

D. Interpretation

In the dual phase shifter configuration, components of the k_x distribution which are faster than average ($\delta k_x > 0$) on their first pass of the phase shifter are slower than average ($\delta k_x < 0$) by the same amount on their second pass. That is why the dual phase shifter is nondispersive in two respects. In addition to being independent of the k_z component (which is already the case for the single phase shifter), the phase shift is also, to first order, constant for all components of the k_x distribution. The interfering wave packets have not only the same position but also the same shape.

Being truly nondispersive and nondefocusing the configuration resembles topological phase measurements like the Aharonov-Bohm phase [10] and can likewise accept a large wavelength spread of incident neutrons [9]. The acceptable wavelength spread is only constrained by the range of Bragg angles the interferometer can accommodate and at which neutrons can traverse the entire sample depth.

V. MEASUREMENTS

We made a proof-of-the-principle b_c measurement with a nondispersive silicon dual phase shifter [Fig. 2(a)] of the S18 neutron interferometer setup of the Institut Laue Langevin in Grenoble [15]. A symmetric 220 LLL interferometer was operated with 2.36 Å neutrons at a Bragg angle of 38°, allowing a 25-mm-thick single phase shifter in the first gap. However, the beam broadening on passing the mirror blade over the Borrmann fan reduced the maximum sample thickness usable in the second gap to 18 mm. A monolithic 18-mm-thick and 93-mm-long silicon dual phase shifter was hence fabricated with a 6-mm-wide groove in the middle to accommodate the mirror blade. Thus the dual shifter phase was only 1.44 (instead of the theoretical 2) times the single shifter phase. An auxiliary 4-mm-thick aluminium phase flag (cf. Fig. 6) was used to record the interference fringes. On placing the sample on one path, the interference contrast was reduced to about 96% of the empty interferometer contrast. We attribute this drop of contrast to incoherent scattering as the total diagonal flight path through silicon sample amounts to 58 mm. The intrinsic drop of contrast accompanying the large phase shift of about 1.6×10^5 deg is practically zero (cf. Fig. 9).

The phases extracted from interferograms acquired at several rotations ε and tilts γ of the sample were fitted to parabolic curves (Fig. 10). The sample was then set to the correct orientation (ε and $\gamma = 0$) where the phase magnitude exhibited a minimum.

A large number of successive sample-in and- out interferometric scan pairs were then recorded alternately for paths I and II. It took half a day for the phase shift to stabilize to a constant value (cf. Fig. 11). A typical path I–path II interferogram pair is depicted in Fig. 12. An average over 13 pairs of stable interference patterns yielded a II–I phase shift $= -(456 \times 720 - 256.7) \pm 0.30$ deg. The interference order (456) was deduced from previous b_c measurements for Si [4].

The Si b_c value of 4.1 479 ± 0.0 023 fm was thus arrived at after adding a correction of 0.009137 fm for air, the major

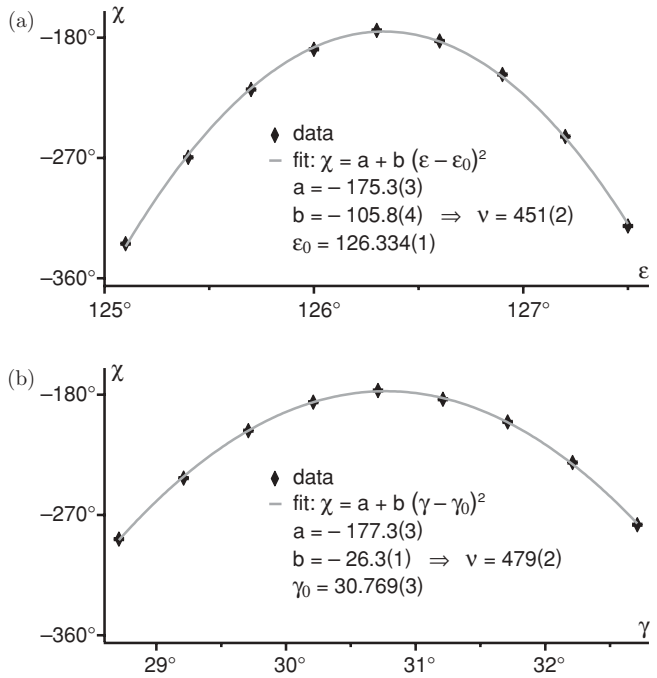

FIG. 10. Measured phase of the dual phase shifter in beam path II versus alignment angles ε and γ. Each curve has been acquired with the other angle set to its optimal value. The given errors contain the statistical part only. The curves have random offset since there was no need to subtract the sample-out phase for alignment purposes.

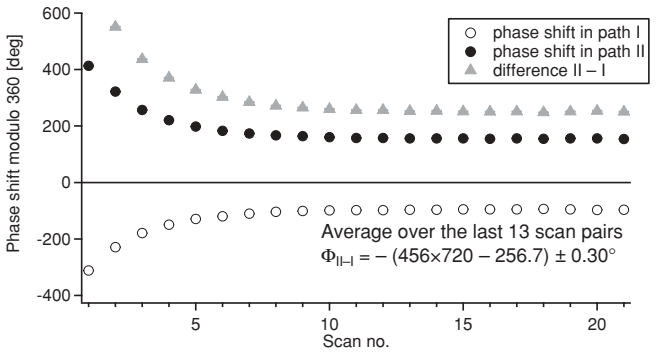

FIG. 11. Successive phase shift measurements (sample in minus out) of the dual phase shifter in beam I and beam II. It took the first measurements half a day for the system to stabilize. The final result was taken as an average over the stable scans.

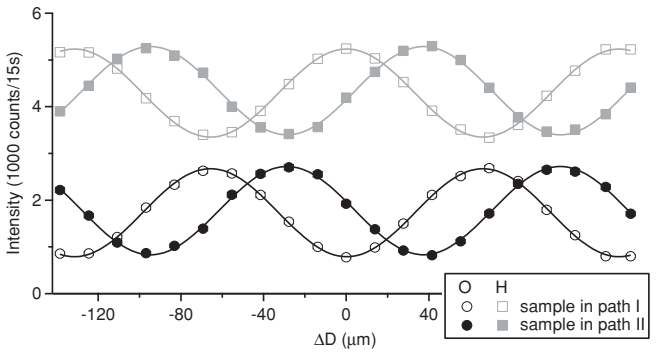

FIG. 12. Typical interferograms recorded with the nondispersive dual phase shifter placed alternately on path I and path II.

part of the b_c error arising from the metrologically observed variation of 10 μm in the sample thickness. The correction of -1.01×10^{-5} fm to b_c due to refraction at the air-sample interfaces is too small in comparison.

If the interference order ν is not known from previous measurements one can in principle deduce it from the curvature of the parabola scans. Writing the theoretical alignment curve (9) in degree units

$$\chi_d = \chi_{d0}\left[1+\left(\cot^2\theta+\frac{1}{2}\right)\left(\frac{\pi}{180}\right)^2(\varepsilon-\varepsilon_0)^2\right] \times\left[1+\frac{1}{2}\left(\frac{\pi}{180}\right)^2(\gamma-\gamma_0)^2\right]-\nu 360^\circ \tag{54}$$

and comparing it with the fit functions $\chi_d(\varepsilon) = a + b_\varepsilon(\varepsilon - \varepsilon_0)^2$ and $\chi_d(\gamma) = a + b_\gamma(\gamma - \gamma_0)^2$ we identify

$$a = \chi_{d0} - \nu 360, \tag{55}$$

$$b_\varepsilon = \chi_{d0}\left(\cot^2\theta+\frac{1}{2}\right)\left(\frac{\pi}{180}\right)^2, \tag{56}$$

$$b_\gamma = \chi_{d0}\frac{1}{2}\left(\frac{\pi}{180}\right)^2, \tag{57}$$

$$\nu = \lfloor \chi_{d0}/360^\circ \rfloor. \tag{58}$$

The curvatures $b_{\varepsilon,\gamma}$ contain the full phase shift χ_{d0} and not just χ_{d0} modulo 360°. If the curvatures can be determined with sufficient accuracy they directly yield the interference order. Due to slightly curved sample surfaces and thermal instabilities we observed some variations in the curvatures and could determine the interference order only as $\nu = 466 \pm 27$ by averaging over 25 measurements. For a precise determination one would need to reduce the systematic errors and/or use thinner samples. Nevertheless, the result agrees with the expected interference order of 456 and confirms that the dual phase shifter doubles the single phase shift.

VI. CONCLUSION

Rauch *et al.*'s [2] nondispersive phase shifter configuration afforded precise interferometric determination of neutron coherent scattering lengths. Ioffe and Vrana [3] and Ioffe *et al.* [4] improved the precision further by an order of magnitude by alternating the phase shifter between the two paths of the interferometer.

We have presented here a dual nondispersive phase shifter which is more nondispersive than the single "nondispersive" phase shifter by several orders of magnitude. This advantage will be especially interesting for cold neutron interferometry. Even for thermal neutrons the dual phase shifter generates double the phase with a null wave-packet displacement and substantially simplifies the angular alignment. One may envisage an interferometer setup dedicated to b_c measurements, operating at a large Bragg angle and with a mirror blade cut to accommodate a nongrooved dual phase shifter or a container cell for liquid and gaseous materials.

ACKNOWLEDGMENTS

Fruitful discussions with Gerald Badurek, Erwin Jericha, and Helmut Rauch are gratefully acknowledged. We thank

Rudolf Loidl and Helmut Rauch for participation in the interferometric experiment with the Si dual phase shifter and Sohrab Abbas for partaking in its analysis. The work has been supported by the project P18943 of the Austrian Science Fund (FWF). One of us (AGW) is thankful to DST (Department of Science and Technology), India, for partially funding his short visit to ILL during which the present work was initiated.

[1] H. Rauch and S. A. Werner, *Neutron Interferometry* (Clarendon, Oxford, 2000).
[2] H. Rauch, E. Seidl, D. Tuppinger, D. Petrascheck, and R. Scherm, Z. Phys. B **69**, 313 (1987).
[3] A. Ioffe and M. Vrana, Phys. Lett. A **231**, 319 (1997).
[4] A. Ioffe, D. L. Jacobson, M. Arif, M. Vrana, S. A. Werner, P. Fischer, G. L. Greene, and F. Mezei, Phys. Rev. A **58**, 1475 (1998).
[5] A. G. Wagh and S. Abbas, J. Res. Natl. Inst. Stand. Technol. **110**, 237 (2005).
[6] D. Petrascheck, Phys. Rev. B **35**, 6549 (1987).
[7] D. Petrascheck and R. Folk, Phys. Status Solidi A **36**, 147 (1976).
[8] H. Rauch, H. Wölwitsch, H. Kaiser, R. Clothier, and S. A. Werner, Phys. Rev. A **53**, 902 (1996).
[9] G. Badurek, H. Weinfurter, R. Gähler, A. Kollmar, S. Wehinger, and A. Zeilinger, Phys. Rev. Lett. **71**, 307 (1993).
[10] Y. Aharonov and D. Bohm, Phys. Rev. **115**, 485 (1959).
[11] U. Bonse and W. Graeff, *X-Ray Optics* (Springer-Verlag, Heidelberg, 1977), pp. 93–123.
[12] A. G. Wagh and V. C. Rakhecha, Prog. Part. Nucl. Phys. **37**, 485 (1996).
[13] H. Lemmel, Phys. Rev. B **76**, 144305 (2007).
[14] C. Pruner, M. Fally, R. A. Rupp, R. P. May, and J. Vollbrandt, Nucl. Instrum. Methods Phys. Res. A **560**, 598 (2006).
[15] A. G. Wagh, S. Abbas, H. Rauch, H. Lemmel, and R. Loidl, Experimental Report 3-15-58, Institut Laue Langevin, 2009 (to be published).